

Valence state determines the band magnetocrystalline anisotropy in 2D rare-earth/noble-metal compounds

M. Blanco-Rey,^{1,2} R. Castrillo-Bodero,³ K. Ali,^{2,3} P. Gargiani,⁴ F. Bertran,⁵
P.M. Sheverdyaeva,⁶ J.E. Ortega,^{7,3,2} L. Fernandez,^{7,3} and F. Schiller^{3,2}

¹ *Departamento de Polímeros y Materiales Avanzados: Física, Química y Tecnología, Universidad del País Vasco UPV-EHU, 20018 San Sebastián, Spain*
² *Donostia International Physics Center, E-20018 Donostia-San Sebastián, Spain*

³ *Centro de Física de Materiales CSIC/UPV-EHU-Materials Physics Center, E-20018 San Sebastián, Spain*

⁴ *ALBA Synchrotron Light Source, Carretera BP 1413 km 3.3, 08290 Cerdanyola del Vallès, Spain*

⁵ *Synchrotron SOLEIL, CNRS-CEA, L'Orme des Merisiers, Saint-Aubin-BP48, 91192 Gif-sur-Yvette, France*

⁶ *Instituto di Struttura della Materia, Consiglio Nazionale delle Ricerche, 34149 Trieste, Italy*

⁷ *Departamento de Física Aplicada I, Universidad del País Vasco UPV/EHU, E-20018 San Sebastián, Spain*

(Dated: January 26, 2022)

In intermetallic compounds with zero-orbital momentum ($L = 0$) the magnetic anisotropy and the electronic band structure are interconnected. Here, we investigate this connection on divalent Eu and trivalent Gd intermetallic compounds. We find by X-ray magnetic circular dichroism an out-of-plane easy magnetization axis in 2D atom-thick EuAu₂. Angle-resolved photoemission and density-functional theory prove that this is due to strong $f-d$ band hybridization and Eu²⁺ valence. In contrast, the easy in-plane magnetization of the structurally-equivalent GdAu₂ is ruled by spin-orbit-split d -bands, notably Weyl nodal lines, occupied in the Gd³⁺ state. Regardless of the L value, we predict a similar itinerant electron contribution to the anisotropy of analogous compounds.

I. INTRODUCTION

The spin-orbit coupling (SOC) is responsible for the splitting of a $4f^n$ orbital into multiplet states $|JJ_z\rangle$ defined by the total angular momentum J and its projection J_z on the magnetization direction. If these levels are accessible by the crystal field energies, quenching of $\langle J_z \rangle$ can occur. The orientation dependence of this mixing of states is at the origin of the strong magnetocrystalline anisotropy of systems based in rare earths (RE) [1, 2]. In recent years, magnets in the zero-dimensional (0D) limit have been successfully realized using REs, either as isolated ad-atoms [3–7] or as centers in organic molecules [8–14]. Prior to these achievements it was known that the $4f$ electron shell confers to bulk intermetallic RE compounds uniaxial anisotropy and high Curie temperatures T_C (and consequently large coercive fields) [15], where the magnetic coupling follows a RKKY mechanism [16]. In two-dimensional (2D) rare-earth/noble-metal (RE/NM) surface compounds large T_C values are retained [17–22]. Anisotropy is a requisite for stable long-range magnetic ordering in 2D [23–25]. Magneto-optic Kerr effect (MOKE) and X-ray magnetic circular dichroism (XMCD) studies reveal that the magnetocrystalline anisotropy in these compounds does not follow a common trend. For example, the HoAu₂ monolayer (ML) grown on Au(111) is strongly anisotropic with out-of-plane (OOP) easy axis, whereas the GdAu₂ one is more easily magnetized in-plane (IP). The HoAu₂ case can be understood in terms of the 5H_8 state given by Hund's rule for $4f^{10}$ (Ho³⁺), since the oblate shape of the orbital and the surface charge distribution favour an OOP easy axis [9, 22]. However, explaining the GdAu₂ anisotropy demands an extension of the model. In fact, the $4f$ shell

of Gd³⁺ is half-filled, i.e. the total orbital quantum number is $L = 0$ ($^8S_{7/2}$ ground state), and the hybridization with the surface bands is negligible, and therefore the anisotropy must have a different origin.

At half-filling $4f^7$, classical dipolar interactions tend to dominate the anisotropy in bulk Gd compounds [26, 27], yet the magnetocrystalline contribution is not fully quenched, as observed in metallic *hcp* Gd [28]. The latter results from the spin polarization of the $5d$ conduction electrons, which are also subject to SOC [29, 30]. This leads to sizable magnetocrystalline anisotropy energy (MAE) values and non-zero orbital momenta [31].

In this work, we show that the magnetocrystalline anisotropy of RE-NM₂ MLs is not defined by the $4f$ single-orbital anisotropy only, but there exists an additional term originated at the itinerant electrons. Since all the compounds of the RE-NM₂ family display similar band dispersion features, the calculations presented here for $L = 0$ systems, namely EuAu₂ and GdAu₂, predict that the itinerant electrons contribute to the MAE with ≈ 1 meV in general and that the RE valence state determines whether this contribution favours an OOP or IP easy axis of magnetization. This means that, for RE materials with a large $4f$ single orbital anisotropy, the total anisotropy will not depend on the band dispersion. For other RE metals, however, the band dispersion may define the magnetic anisotropy. We show that Eu in the EuAu₂ ML on Au(111) behaves as a divalent species and thus it is nominally in a $^8S_{7/2}$ ground state, as Gd³⁺ in the GdAu₂ ML. However, an EuAu₂ ML presents an OOP easy axis of magnetization and MAE = 1.6 meV, in contrast to the IP easy axis observed in GdAu₂. The IP easy axis of GdAu₂ is explained in terms of the SOC lifting degeneracies in dispersive valence bands with Gd(d) character. On the other hand, in divalent EuAu₂ the

Eu(d) states are unoccupied and do not contribute. Instead, the anisotropy is caused by the strong $f-d$ band hybridization.

II. METHODS

A. Experimental Methods

Sample preparation of EuAu₂ has been carried out by thermal deposition of Eu onto a clean Au(111) single crystalline surface. The formation of the monolayer is achieved when a complete layer with moiré is observed in Scanning Tunneling Microscopy (STM), or the surface state emission of the Au(111) Shockley state in angle-resolved photoemission spectroscopy (ARPES) [32, 33] has completely vanished. The substrate temperature is around 675 K for GdAu₂, whereas for EuAu₂ a precise temperature of 575 K is required. The prepared EuAu₂ and GdAu₂ ML systems reveal a $\sqrt{3} \times \sqrt{3}R30^\circ$ atomic arrangement and a long range order moiré lattice with respect to the underlying Au(111) substrate. This superstructure is easily distinguishable in low-energy electron diffraction (LEED) images and serves as a quality indicator in XMCD synchrotron preparations.

The EuAu₂ XMCD measurements were performed at Boreas beamline of the Spanish synchrotron radiation facility ALBA using a 90% circularly polarized light from a helical undulator. The measurements were undertaken at 2-20 K with a variable magnetic field up to ± 6 T. The applied magnetic field \vec{H} was aligned with the photon propagation vector. The XMCD spectrum is the difference between the two X-ray absorption spectroscopy (XAS) spectra recorded with opposite orientation of the magnetic field and/or the circular helicity of the light, which we call μ_+ and μ_- for simplicity. The XMCD signal is proportional to the projection of the magnetization in the direction of the applied magnetic field. At normal light incidence, the field is also normal to the sample surface (out-of-plane geometry) while at grazing incidence (here 70°), the magnetic field is nearly parallel to the surface (in-plane geometry). The magnetization curves are taken by varying continuously the applied field with the sample kept in one of the mentioned geometries for both circular helicities. For normalization issues, at each field value two XAS absorption values were taken, the first one corresponding to the photon energy of the maximum of the XMCD signal, the second one at a slightly lower photon energy prior to the XAS absorption edge. In order to determine the Curie temperature T_C of the material such magnetization curves were taken for several temperatures below and above T_C .

ARPES experiments were taken at CASSIOPEE beamline of SOLEIL synchrotron, France, and at our home laboratory in San Sebastián (Spain) together with the STM and LEED analysis. Photoemission data in San Sebastian were acquired using Helium I α ($h\nu = 21.2$ eV) light. In San Sebastián and at SOLEIL a

channelplate-based display type hemispherical analyzer was used (Specs 150 and Scienta R4000 electron analyzers) with angular and energy resolution set to 0.1° and 40 meV, respectively. At the synchrotron, p -polarized light was used and the sample temperature during measurements was 70 K, while sample temperature during Helium I α ARPES measurements were 120 K. Resonant photoemission spectroscopy (ResPES) is achieved at the Eu $4d \rightarrow 4f$ absorption edge. In such measurements the photoemission signal is resonantly enhanced due to a superposition/interference of the direct photoemission process and an Auger decay and leads to a broad resonant maximum above the $4d$ absorption threshold accompanied by a number of narrow peaks caused by several decay processes that was initially explained for the $4f^7$ configuration of Gd [34] and later for the same configuration of Eu [35]. In mixed-valent Eu compounds slightly different resonant energies [36] can be used to differentiate di- and tri-valent contributions. Here, we used $h\nu = 141$ eV and 146 eV corresponding to two close photon energies in order to minimize photoemission cross-section changes but still resonantly enhance di- or tri-valent signals. The off-resonant energy $h\nu = 130$ eV corresponds to a simple $(4f^7)^8S_{7/2} \rightarrow (4f^7)^7F_J$ photoemission transition. The individual J components cannot be resolved easily at such high photon energies due to worse energy resolution, but have been observed for pure Eu metal at low photon energies [37].

B. Theoretical Methods

Density-functional theory (DFT) calculations were performed in the full-potential linearized augmented plane wave (FLAPW) formalism [38–40] at the GGA+U level to describe strong correlation [41, 42] in the full-localized limit approximation, since the Eu($4f$) orbital is half filled [43]. The Perdew-Burke-Ernzerhof (PBE) exchange and correlation functional [44] was used. The parameter $U = 5.5$ eV is found to match the $4f$ bands binding energies observed in ARPES. In the case of the calculation parameters for GdAu₂, we refer the reader to previous work in Ref. [21], where $U = 7.5$ eV was employed. The lattice constant of the model geometries was fixed to the EuAu₂ experimental value. For the supported models a $\sqrt{3} \times \sqrt{3}R30^\circ$ supercell geometry was used with fcc stacking of atomic planes and an interlayer distance of 2.25 Å between the flat EuAu₂ monolayer and the Au(111) substrate. For the local FLAPW basis, as in previous works with REAu₂, RE- $6s, 4f, 5d$ and Au- $6s, 5d$ electrons were included as valence electrons, and RE- $5s, 5p$ and Au- $5p$ as linear orbitals. Partial wave expansions up to $l_{max} = 8$ and 10 were set inside the Eu and Au muffin-tin spheres of radii 1.43 and 1.48 Å, respectively.

SOC was included in the calculation both self-consistently and in the force theorem perturbative approximation [45–48], i.e. without carrying out further

self-consistent optimization of the charge density, for spins oriented in-plane (X) and out-of-plane (Z) [see Fig. 2(a)]. Using the force theorem, the MAE is computed as the energy difference between the band energies, i.e. it is a rigid-band approximation. The working principles of the method are described in Section III E. The MAE accuracy is highly dependent on the fine details of the band structure, specially the gap openings at band crossings and the Fermi level. Therefore, a fine sampling of the first Brillouin zone (BZ) and the sharpest possible Fermi-Dirac function are required. In this work, the MAE was converged with a tolerance of ~ 0.1 meV using a smearing width $\sigma = 5$ meV for the Fermi level (first-order Methfessel-Paxton method [49]) and a mesh of at least 25×25 k -points, with plane wave expansion cutoffs of 4 and 12 bohr $^{-1}$ for the wavefunctions and potential, respectively.

III. RESULTS AND DISCUSSION

A. Structure Characterization

The EuAu₂ ML is characterized by a hexagonal moiré superstructure visible in the scanning tunneling microscopy (STM) micrograph and the LEED pattern of Fig. 1(a). Similar moiré superstructures are found in other RE/NM metal surfaces [18, 21, 22, 52]. The STM analysis of EuAu₂ yields a moiré superlattice constant of $a_m = (3.3 \pm 0.1)$ nm with a coincidence lattice of $(11.5 \pm 0.3) \times (11.5 \pm 0.3)$ with respect to the Au(111) surface ($a_{Au} = 0.289$ nm), in agreement with LEED. The EuAu₂ ML reveals a $(\sqrt{3} \times \sqrt{3})R30^\circ$ reconstruction on top of the Au(111) surface and a lattice parameter of 0.55 nm. The a_m of EuAu₂ is 10% smaller than the one found in GdAu₂, HoAu₂, or YbAu₂, which show $a_m \approx 3.6$ nm [18, 22].

B. Valency Analysis by ResPES

The ResPES spectrum [see Fig. 1(b)] displays unequivocally the presence of a single Eu²⁺ multiplet peak and no further peaks related to Eu³⁺ revealing the presence of only divalent Eu atoms exclusively located at the EuAu₂ ML. Eu atoms below the surface (either di- or trivalent) would give rise to an additional shifted multiplet [36] that does not appear in the spectra. Therefore, the existence of a single EuAu₂ ML with divalent character is probed.

C. Magnetic Properties by XAS and XMCD

Fig. 1(c) shows the XAS and XMCD spectra of an EuAu₂ ML at the Eu M_{4,5} absorption edges ($T = 3$ K; $\mu_0 H = 6$ T and normal incidence). The XAS line shape confirms the divalent character of the Eu atom in EuAu₂ ML deduced from the ResPES spectra of Fig. 1(b) [see also Supplemental Material (SM) [53] Fig. S4 for comparison to XAS spectrum of trivalent Eu₂O₃]. Magnetization curves of Fig. 1(d) are taken at different geometries and at the photon energy of the maximum M₅ XMCD peak while changing $\mu_0 H$. The out-of-plane magnetization curves with the field applied perpendicular to the surface saturates at approx. 2 T, while the in-plane magnetization curve reaches saturation at much higher applied fields, close to 6 T. This clearly reveals that the easy axis of magnetization is perpendicular to the plane. Magnetization loops were recorded at various temperatures, allowing an Arrot plot estimation [21, 54] of the Curie temperature of the surface compound of $T_C = 13$ K [see inset of Fig. 1(d)]. Further details are found in Fig. S5.

The OOP easy axis of magnetization in EuAu₂ MLs differs from the IP one of GdAu₂ [20, 21], despite of the identical $4f$ electronic configuration ($^8S_{7/2}$) and atomic structure. In the following, we explain this behavior in

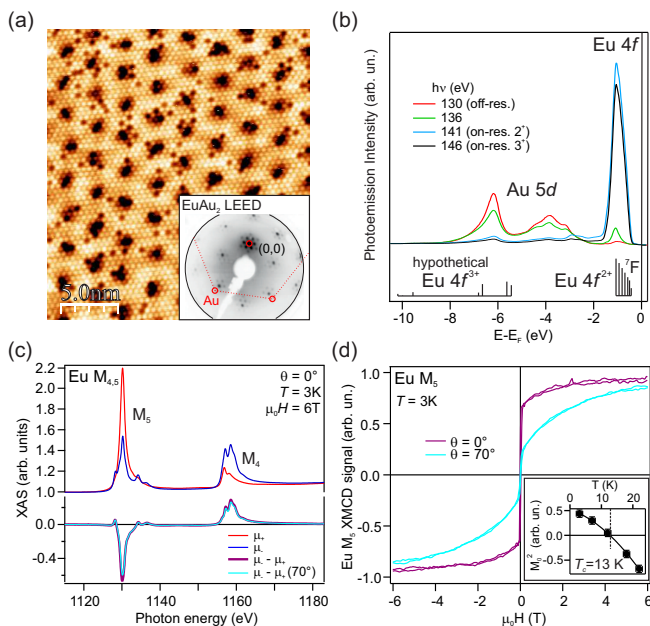


FIG. 1. **Structure, Eu valence and magnetic properties of EuAu₂.** (a) STM image ($U = -2$ V, $I = 200$ pA). Inset: LEED pattern at $E = 40$ eV energy, the red circles mark the Au(111) substrate spots prior to EuAu₂ formation. (b) Resonant photoemission across the $4d \rightarrow 4f$ absorption edge determining the pure monolayer formation of divalent Eu atoms. The final state multiplets are taken from [50, 51]. (c) X-ray absorption at the Eu M_{4,5} edge with circularly left (μ_-) and right (μ_+) polarized light at an applied field of $\mu_0 H = 6$ T and at $T = 3$ K in normal incidence geometry ($\theta = 0$). The difference spectrum (XMCD) is shown for normal and grazing ($\theta = 70^\circ$) incidences. (d) Magnetization curves taken at the Eu M₅ edge in these two geometries and in the inset the corresponding Arrot plot analysis to determine T_C .

terms of their respective band structure measured by ARPES, which exhibits a clear dependence on the valence character of the REs, namely, divalent for Eu and trivalent for Gd. Further analysis by DFT provides insight in the spin-orbit effects on the individual bands.

D. Electronic Structure by ARPES and DFT

Results of ARPES measurements performed on EuAu₂ MLs show the characteristic surface dispersive localized bands with Eu(*d*)-Au(*s*, *p*) character that are commonly found in all REAu₂ surface compounds [19, 21, 22], see Fig. 2(d,e) and SM Figs. S1 and S2. Following the notation of Ref. [22], these valence bands are labelled *A*, *B*, *C*, and *C'*. As already seen in other REAu₂ materials, some of these bands are better detected in the first BZ while other bands gain intensity in higher order BZ's. The 4*f* emissions of Eu are seen in the binding energy range between 1.1 and 0.4 eV, in agreement with ResPES of Fig. 1(b). To better visualize the valence band structure, a low photon energy $h\nu = 21.2$ eV was chosen, where the 4*f* cross-section is relatively low. Signs of hybridization between the localized Eu 4*f* level and the EuAu₂ valence bands are observed as kinks in the linear dispersion of the *C* bands in the second BZ and are marked with arrows in Fig. 2(e) (see also Fig. S2). Such 4*f*-valence band hybridizations have been observed for other Eu-based bulk [55] and in YbAu₂ surface compounds [22]. The *C* band in EuAu₂ is characterized by a nearly conical shape at $\bar{\Gamma}$, with the apex above the Fermi level E_F . DFT band structure calculations for isolated and supported EuAu₂ MLs disclose the intersection above E_F of the *C* band, of d_{xy} character, with bands of $d_{x^2-y^2}$ and $d_{xz,yz}$ character, as shown in Fig. 2(c). These band crossings occur below (above) the Fermi energy for trivalent (divalent) RE ions [21, 22]. Adding the 3 ML Au(111) substrate slab provide additional dispersive bands [21, 22], which cause an upward shift of ≈ 0.1 eV in the RE(*d*)-Au(*s*) hybrid band manifold, and a strong renormalization of 4*f* levels. Indeed, in the calculated free-standing EuAu₂ band structure the 4*f* states lie ≈ 0.7 eV lower. The 4*f* band of EuAu₂ is half-filled but, as the individual bands are heavily split by hybridization with the *A* and *C* bands, it shows some degree of dispersion across the BZ. In contrast, Gd(4*f*) orbital in GdAu₂ barely interacts with the surrounding metal, showing a small crystal field splitting and no significant dispersion (see SM Fig. S3).

E. Force Theorem Analysis

SOC at the crossings of the two-dimensional RE(*d*)-Au(*s*) bands are sources of anisotropy that we characterize by DFT in the following. The SOC matrix element for two electrons belonging to orbitals of the same shell is

$$\langle lm\sigma|\xi_l\mathbf{l}\cdot\mathbf{s}|lm'\sigma'\rangle \quad (1)$$

where \mathbf{l} and \mathbf{s} are the one-electron orbital and spin momentum operators; l , m and σ indices label the eigenstates of \mathbf{l} , l_z , and \mathbf{s} , respectively; and ξ_l is the SOC strength, which is approximately constant for all the electrons in each l -shell. Intershell SOC is negligible. For hydrogenic atomic orbitals, these matrix elements are analytical and have been tabulated [56, 57]. Selected combinations of m values and spin orientations give non-zero matrix elements. A second-order perturbative treatment of the SOC hamiltonian term shows that this behaviour is inherited by hybrid bands of an extended system [58–64]. In such case, degeneracy lifting at band crossings obeys the rules imposed by the crystallographic symmetry of the system and the orbital symmetry of the bands for a given orientation of the spins.

In the so-called force theorem approach, where the SOC correction enters non-self-consistently in the DFT calculation, the MAE is obtained from the spin-orientation-dependent band energy contribution to the total energy of the system [45, 47]:

$$\text{MAE} = \sum_{kn} \epsilon_{kn}^X f_{FD}(\epsilon_{kn}^X - E_F^X) - \sum_{kn} \epsilon_{kn}^Z f_{FD}(\epsilon_{kn}^Z - E_F^Z) \quad (2)$$

where the sum runs over the eigenenergies $\epsilon_{kn}^{\hat{s}_a}$ (k and n are the k -point and band indices, respectively), f_{FD} is the Fermi-Dirac function, and $E_F^{\hat{s}_a}$ are the Fermi energies for the spin orientations $\hat{s}_a = Z$ (out-of-plane) and X [the in-plane direction along nearest RE atoms, shown in Fig. 2(a)]. Azimuthal dependence of the MAE is small. According to this equation, non-zero contributions to the MAE are generated at band crossings that become gapped for one spin orientation, but not for the other. The final easy-axis direction results from the integration of all individual gap contributions, of positive and negative small values, over occupied states. At crossings of fully occupied bands, the energy dispersion around the degeneracy point has to be asymmetrical in order to have a sizable contribution to MAE, otherwise band energies around the gapped feature will cancel out each other. If the degeneracy lifting occurs exactly at the Fermi level, the contribution to the MAE will be large [47, 65].

A spectral analysis of Eq. 2 is not possible, as the Fermi energy depends on the spin orientation. Instead, the common practice is to plot MAE *vs.* N_e , i.e. $\text{MAE}(N_e)$, where N_e is the number of electrons with respect to the neutral case ($N_e = 0$) calculated as an integral over the density of states of the system for each spin orientation, i.e. each N_e value provides $E_F^{X,Z}(N_e)$ values [64–68]. Therefore, the $\text{MAE}(N_e)$ curve allows to assign a positive or a negative MAE contribution to the region of the energy range close to $E_F^{X,Z}(N_e)$. As the Fermi energy fluctuation with the spin direction is small (a few meV), we use the $E_F(N_e)$ value calculated without SOC to guide the eye in the graphs. The value obtained at neutrality, $\text{MAE}(N_e = 0)$, corresponds to the expected anisotropy of the system. This type of MAE analysis relies on the validity of the force theorem approximation, namely, it

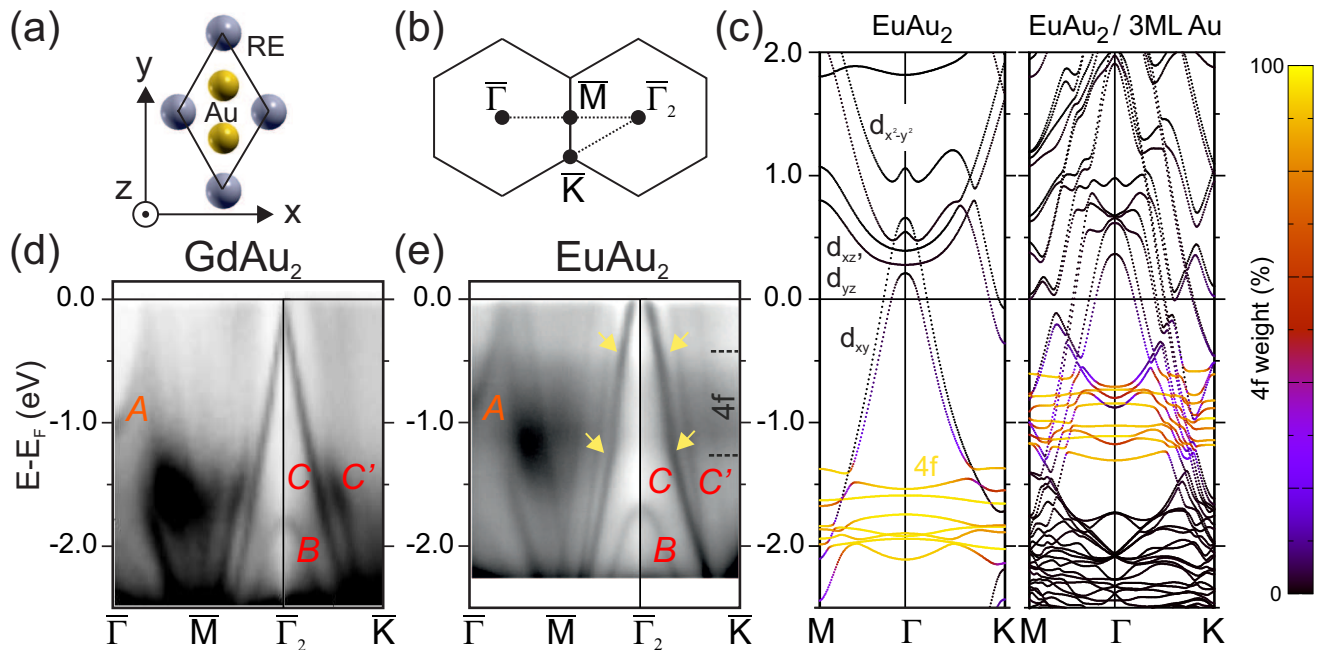


FIG. 2. **Band structures of GdAu₂ and EuAu₂.** (a) Model of the REAu₂ ML unit cell. (b) Path in the reciprocal space of the band structures measured by ARPES at photon energy $h\nu = 21.2$ eV for GdAu₂ (d) and EuAu₂ (e). (c) Band structure from DFT calculations along the indicated high-symmetry direction for a EuAu₂ monolayer, both free-standing (left) and on 3ML Au(111) slab-supported (right). The Eu 4f contribution to the states is indicated in a colored scale.

assumes that there are only minor changes in the electron density (essentially, loss of collinearity) caused by the effect of SOC [46, 47]. Despite the two REAu₂ compounds under study being heavy-atom systems, by comparing to fully self-consistent calculations of the band structures with SOC, we find that the force theorem properly accounts for the spin-orbit induced gaps in an energy range of several eV around the Fermi energy (see SM Figs. S6 and S7 for GdAu₂ and EuAu₂, respectively).

1. GdAu₂

We apply this analysis to the band structure of free-standing and supported GdAu₂ MLs, shown in Fig. 3(b-c). The band crossings labelled α and α' in the figures are degenerate for in-plane magnetization, but split by OOP magnetization. Fig. 3(a) panels shows, as a guide for the eye, the orbital characters and spin polarities in the absence of SOC for free-standing GdAu₂. The α and α' features are crossings between d_{xy} and $d_{x^2-y^2}$ ($m = \pm 2$) with *equal* spin polarization, a situation where the matrix element Eq. 1 foresees splitting by OOP magnetization. The Weyl nodal line β [69], which is a ring-shaped crossing around the Γ point between d_{xy} and $d_{x^2-y^2}$ bands with *opposite* spin polarization [see Fig. 3(a)], is split by in-plane magnetization according to Eq. 1.

Fig. 3(d) shows the obtained MAE(N_e). The curves $E_F(N_e) - E_F(0)$ without SOC, shown in the SM Fig. S9 establish an approximate mapping between band fillings

and binding energies [a few discrete values are given also in the right-hand side axes of Fig. 3(b,c)]. For GdAu₂ close to neutrality ($N_e = 0$) the essential contributions to the MAE are those of α, α' and β features. In the free-standing case, the β nodal ring results in the net sharp MAE peak of negative values in the dashed red line at $N_e = -0.9$ (i.e. contributing to IP easy axis of magnetization), whereas features α and α' contribute to the OOP easy magnetization axis with peaks of positive MAE at $N_e = -1$ and just above $N_e = 0$ in the red dashed curve of Fig. 3(d). At neutrality we obtain an OOP easy axis with MAE(0) = 0.17 meV.

The same features α, α' and β appear for GdAu₂/3ML Au(111), albeit at binding energies higher by ~ 0.1 eV [see Figs. 3(b,c)], which also result in positive and negative contributions to the MAE around the neutrality point. The β line causes the in-plane peak at $N_e = -0.5$ (solid blue line), and α and α' contribute to the OOP magnetization easy axis with positive-valued MAE peaks at $N_e = -1.3$ and 0.8, respectively. At the neutrality point we find MAE(0) = -0.9 meV, i.e. IP easy axis of magnetization, same as observed experimentally. This is due to the contribution of the β gapped line, which dominates over α and α' single-point gaps at Γ , aided by the fact that the β gapped line lies closer to E_F in the supported case. The contribution of the GdAu₂ 4f⁷ electrons to the anisotropy lies within the force theorem error, since the departure from sphericity of this orbital is negligible when embedded in the alloy (in other words, the Gd(4f) spin density cloud would be almost insen-

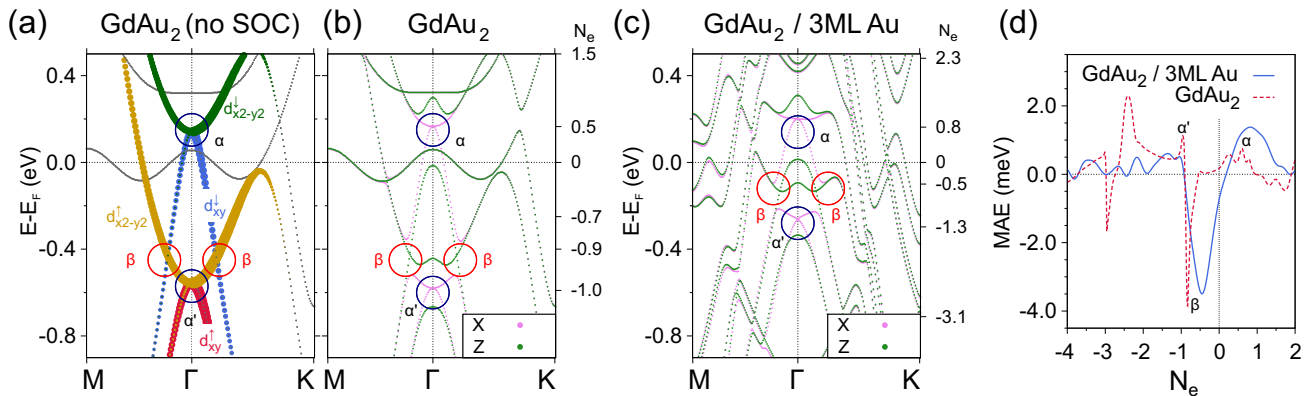


FIG. 3. **Band structure and MAE of GdAu₂ as a function of band filling.** (a) Orbital and spin characters of free-standing GdAu₂ bands in the absence of SOC. Band structure of a free-standing (b) and supported (c) GdAu₂ ML for spins aligned to the X (violet) and Z (green) directions in the force theorem approximation, each calculation referred to its own Fermi level. The SOC-induced gaps at the band crossings relevant to the MAE are indicated with circles labelled α , α' and β . The right-hand side axes show the corresponding band filling, i.e. the number of electrons N_e referred to charge neutrality. (d) MAE as a function of N_e for free-standing (solid) and supported (dashed) GdAu₂. Positive (negative) MAE values mean OOP (IP) easy magnetization axis.

sitive to the applied field orientation, as shown in SM Fig. S3). Therefore, we attribute the experimental easy magnetization plane essentially to the MAE contribution of the dispersive Gd(d)-Au(s) bands.

2. EuAu₂

Next, we apply the force theorem methodology to the EuAu₂ bands. Bare inspection of the band structures of both free-standing and supported EuAu₂ MLs rules out the possibility of the anisotropy being dominated by the SOC effects on the Eu(d)-Au(s) hybrid bands for two reasons: (i) due to the divalent character of Eu, the d_{xy} and $d_{x^2-y^2}$ band crossings relevant for MAE are unoccupied [see Fig. 2(c)] and thus they cannot contribute to the observed anisotropy, and (ii) the f -band is heavily broadened by hybridization, with individual bands showing significant dispersion and spin orientation dependence [see SM Fig. S3(d)].

The force theorem Eq. 2 applied to the $U = 5.5$ eV band structures yields an OOP easy magnetization axis both for free-standing and supported EuAu₂, with $\text{MAE}(0) = 1.0$ and 1.54 meV, respectively [these are, respectively, the values taken by the thick red dashed and blue solid curves, at neutrality in Fig. 4(a)]. The MAE peaks due to α' , β and α band crossing features are visible in the free-standing EuAu₂ bands above the charge neutrality level (see also Fig. S8). For EuAu₂/3ML Au(111), Fig. 4(b) shows two large broad peaks at each $\text{MAE}(N_e)$ curve, which take values $\simeq \pm 0.1$ eV at the electron filling ranges that correspond to the binding energy ranges where the hybridized $4f$ bands lie. The peak pairs account for the filling of the SOC-split band manifolds $4f_{7/2}$ and $4f_{5/2}$. In the calculation with $U = 5.5$ eV, these peaks occur at $N_e = -10$ and -5 , respectively, corre-

sponding to binding energies close to -1 eV [see also SM Fig. S9(b,c)]. These bands yield a non-negligible positive residual contribution to $\text{MAE}(0)$ by virtue of the $f - d$ hybridization. In a single-ion picture, this would be interpreted as a loss of sphericity of the half-filled $4f$ shell, which acquires a net non-zero $\langle L \rangle$ [9]. The SM Fig. S3 shows the magnetization distribution projected on \hat{s}_a [$m_{\hat{s}_a}(\mathbf{r})$] of the Eu($4f$) shell embedded in the free-standing alloy monolayer, obtained by integration of the Kohn-Sham states in the binding energy range between -2.25 and -1.25 eV. The magnetization anisotropy distribution $m_X(\mathbf{r}) - m_Z(\mathbf{r})$ takes positive and negative values in-plane and out-of-plane, respectively, which can be interpreted as the Eu(f) orbital spin density tendency to become deformed along the applied field direction. Note that the same quantity integrated for Gd(f) between -10 and -8.5 eV is an order of magnitude smaller.

The $4f$ contribution to the MAE of EuAu₂ can be further probed by modifying the U correlation parameter. We have carried out force theorem analyses for supported EuAu₂ with $U = 3.5$ and 7.5 eV. When U is decreased, the MAE energy is increased by $\simeq 1$ meV and when U is increased, the easy axis of magnetization remains out-of-plane, but the $\text{MAE}(0)$ value is reduced (see Fig. 4). The densities of states [SM Fig. S9(d)] show that a larger U value implies less hybridization between the $4f$ electrons and the hybrid bands of d character crossing the Fermi level. Indeed, for $U = 7.5$ eV the $4f$ band lies below $E_F - 1.5$ eV, i.e. close to the Au substrate states and below the d_{xy} band. For $U = 3.5$ eV, however, the $4f$ band is centred at $E_F - 0.5$ eV, producing hybrid $f - d$ states close to the Fermi level. This shows that the degree of $f - d$ hybridization drives the MAE behaviour of EuAu₂.

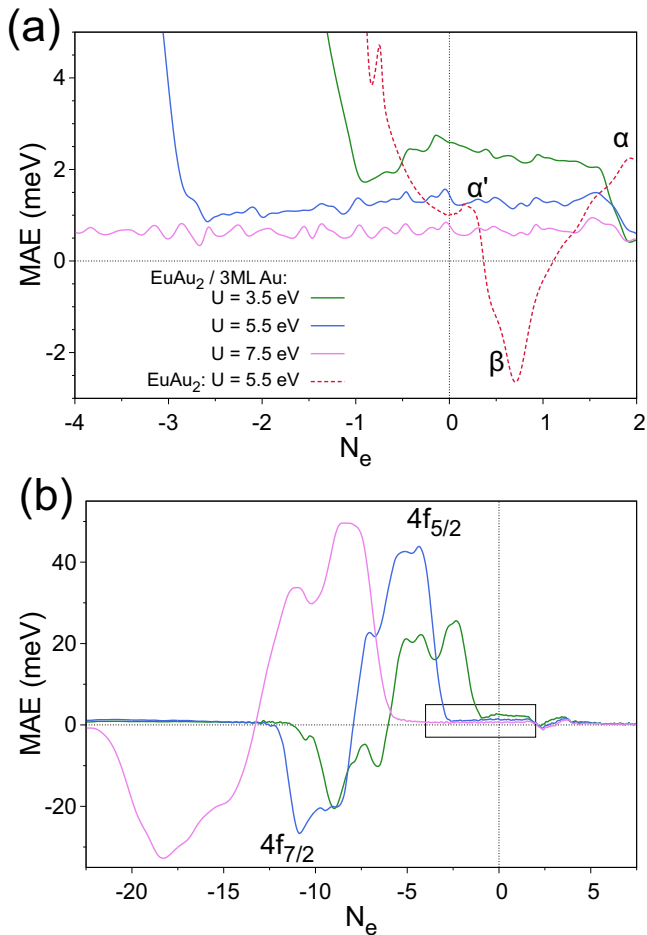


FIG. 4. MAE of EuAu_2 as a function of band filling (a) MAE as a function of N_e for free-standing (solid blue) and supported (dashed red) EuAu_2 calculated with $U = 5.5$ eV close to the neutrality condition $N_e = 0$. Positive (negative) MAE values contribute to the OOP (IP) easy magnetization axis. Additional solid curves show the results for $\text{EuAu}_2/3\text{ML Au}$ with other U values. (b) Same curves in a wider N_e to show the large contributions of $4f$ electrons, switching the easy axis of magnetization from IP (negative MAE) to OOP (positive MAE). The rectangle corresponds to the close-up shown in panel (a).

IV. CONCLUSIONS

To summarize, our XMCD experiments have determined that a EuAu_2 ML on Au(111) shows out-of-plane easy magnetization axis. Using photoemission experiments combined with DFT calculations, we show that this is a consequence of the Eu^{2+} valence state and the $f-d$ band hybridization. In contrast, the easy magnetization plane of GdAu_2 ML is explained by Gd^{3+} valence and spin-orbit splitting of the point and line degeneracies of bands with d_{xy, x^2-y^2} character. The role of the RE valence is to determine whether these specific states are occupied or empty. This model of the contribution of the itinerant electrons to the magnetocrystalline anisotropy

is a general result for the REAu_2 family of monolayer compounds. For $\text{RE}=\text{Eu}, \text{Gd}$ this is the only mechanisms at work, since the $4f$ orbital is half-filled, i.e. $L = 0$. For RE atoms with non-zero L quantum numbers, there is a single-ion anisotropy that results from the interplay between spin-orbit and crystal-field splittings of the $4f$ multiplet. For example, this multiplet mechanism dominates the OOP easy magnetization axis behaviour in HoAu_2 , where the valence is Ho^{3+} [22]. We predict the itinerant electrons to yield MAE values of ≈ 1 meV in REAu_2 monolayers, irrespective of the L value. Therefore, the band and multiplet mechanisms may eventually compete.

ACKNOWLEDGMENTS

Discussions with the late J.I. Cerdá are warmly thanked. Financial support from projects MAT-2017-88374-P, PID2020-116093RB-C44 and PID2019-103910GB-I00, funded by MCIN/AEI/10.13039/501100011033/, the Basque Government (grants IT-1255-19, IT1260-19), and the University of the Basque Country (UPV/EHU) (grant GIU18/138) is acknowledged. Computational resources were provided by DIPIC. The SOLEIL based research leading to the results has been supported by the project CALIPSOplus under Grant Agreement 730872 from the EU Framework Programme for Research and Innovation HORIZON 2020. L.F. acknowledges financial support from the EU's Horizon 2020 research and innovation programme under the Marie Skłodowska-Curie grant agreement MagicFACE No 797109.

- [1] K. H. J. Buschow and F. de Boer, *Physics of Magnetism and Magnetic Materials* (Kluwer Academic / Plenum Publishers, New York, 2003).
- [2] R. Skomski and D. Sellmyer, *Journal of Rare Earths* **27**, 675 (2009).
- [3] F. Donati, A. Singha, S. Stepanow, C. Wäckerlin, J. Dreiser, P. Gambardella, S. Rusponi, and H. Brune, *Phys. Rev. Lett.* **113**, 237201 (2014).
- [4] F. Donati, S. Rusponi, S. Stepanow, C. Wäckerlin, A. Singha, L. Persichetti, R. Baltic, K. Diller, F. Patthey, E. Fernandes, J. Dreiser, Ž. Šljivančanin, K. Kummer, C. Nistor, P. Gambardella, and H. Brune, *Science* **352**, 318 (2016).
- [5] A. Singha, R. Baltic, F. Donati, C. Wäckerlin, J. Dreiser, L. Persichetti, S. Stepanow, P. Gambardella, S. Rusponi, and H. Brune, *Phys. Rev. B* **96**, 224418 (2017).
- [6] F. D. Natterer, F. Donati, F. m. c. Patthey, and H. Brune, *Phys. Rev. Lett.* **121**, 027201 (2018).
- [7] F. Donati, S. Rusponi, S. Stepanow, L. Persichetti, A. Singha, D. M. Juraschek, C. Wäckerlin, R. Baltic, M. Pivetta, K. Diller, C. Nistor, J. Dreiser, K. Kummer, E. Velez-Fort, N. A. Spaldin, H. Brune, and P. Gambardella, *Phys. Rev. Lett.* **124**, 077204 (2020).
- [8] N. Ishikawa, M. Sugita, and W. Wernsdorfer, *Angewandte Chemie International Edition* **44**, 2931 (2005).
- [9] J. D. Rinehart and J. R. Long, *Chem. Sci.* **2**, 2078 (2011).
- [10] M. J. Martínez-Pérez, S. Cardona-Serra, C. Schlegel, F. Moro, P. J. Alonso, H. Prima-García, J. M. Clemente-Juan, M. Evangelisti, A. Gaita-Ariño, J. Sesé, J. van Slageren, E. Coronado, and F. Luis, *Phys. Rev. Lett.* **108**, 247213 (2012).
- [11] M. Mannini, F. Bertani, C. Tudisco, L. Malavolti, L. Poggini, K. Misztal, D. Menozzi, A. Motta, E. Otero, P. Ohresser, P. Saintavit, G. G. Condorelli, E. Dalcanale, and R. Sessoli, *Nature Communications* **5**, 4582 (2014).
- [12] B. W. Heinrich, L. Braun, J. I. Pascual, and K. J. Franke, *Nano Letters* **15**, 4024 (2015).
- [13] A. Chiesa, F. Cugini, R. Hussain, E. Macaluso, G. Allodi, E. Garlatti, M. Giansiracusa, C. A. P. Goodwin, F. Ortu, D. Reta, J. M. Skelton, T. Guidi, P. Santini, M. Solzi, R. De Renzi, D. P. Mills, N. F. Chilton, and S. Carretta, *Phys. Rev. B* **101**, 174402 (2020).
- [14] M. Briganti, E. Lucaccini, L. Chelazzi, S. Ciattini, L. Sorace, R. Sessoli, F. Totti, and M. Perfetti, *Journal of the American Chemical Society* **143**, 8108 (2021).
- [15] Givord, D., Laforest, J., Li, H. S., Liénard, A., de la Bâthie, R. Perrier, and Tenaud, P., *J. Phys. Colloques* **46**, C6 (1985).
- [16] K. Buschow, *Reports on Progress in Physics* **42**, 1373 (1979).
- [17] M. Corso, M. J. Verstraete, F. Schiller, M. Ormaza, L. Fernández, T. Greber, M. Torrent, A. Rubio, and J. E. Ortega, *Phys. Rev. Lett.* **105**, 016101 (2010).
- [18] M. Corso, L. Fernández, F. Schiller, and J. E. Ortega, *ACS Nano* **4**, 1603 (2010).
- [19] M. Ormaza, L. Fernández, S. Lafuente, M. Corso, F. Schiller, B. Xu, M. Diakhate, M. J. Verstraete, and J. E. Ortega, *Phys. Rev. B* **88**, 125405 (2013).
- [20] L. Fernández, M. Blanco-Rey, M. Ilyn, L. Vitali, A. Magaña, A. Correa, P. Ohresser, J. E. Ortega, A. Ayuela, and F. Schiller, *Nano Letters* **14**, 2977 (2014).
- [21] M. Ormaza, L. Fernández, M. Ilyn, A. Magaña, B. Xu, M. J. Verstraete, M. Gastaldo, M. A. Valbuena, P. Gargiani, A. Mugarza, A. Ayuela, L. Vitali, M. Blanco-Rey, F. Schiller, and J. E. Ortega, *Nano Letters* **16**, 4230 (2016).
- [22] L. Fernandez, M. Blanco-Rey, R. Castrillo-Bodero, M. Ilyn, K. Ali, E. Turco, M. Corso, M. Ormaza, P. Gargiani, M. A. Valbuena, A. Mugarza, P. Moras, P. M. Sheverdyaeva, A. K. Kundu, M. Jugovac, C. Laubschat, J. E. Ortega, and F. Schiller, *Nanoscale* **12**, 22258 (2020).
- [23] N. D. Mermin and H. Wagner, *Phys. Rev. Lett.* **17**, 1133 (1966).
- [24] V. Berezinskii, *Soviet Physics JETP-USSR* **32**, 493+ (1971).
- [25] J. M. Kosterlitz and D. J. Thouless, *Journal of Physics C: Solid State Physics* **6**, 1181 (1973).
- [26] D. J. W. Geldart, P. Hargraves, N. M. Fujiki, and R. A. Dunlap, *Phys. Rev. Lett.* **62**, 2728 (1989).
- [27] M. Rotter, M. Loewenhaupt, M. Doerr, A. Lindbaum, H. Sassik, K. Ziebeck, and B. Beuneu, *Phys. Rev. B* **68**, 144418 (2003).
- [28] J. J. M. Franse and R. Gersdorf, *Phys. Rev. Lett.* **45**, 50 (1980).
- [29] M. Wietstruk, A. Melnikov, C. Stamm, T. Kachel, N. Pontius, M. Sultan, C. Gahl, M. Weinelt, H. A. Dürr, and U. Bovensiepen, *Phys. Rev. Lett.* **106**, 127401 (2011).
- [30] M. Colarieti-Tosti, S. I. Simak, R. Ahuja, L. Nordström, O. Eriksson, D. Åberg, S. Edvardsson, and M. S. S. Brooks, *Phys. Rev. Lett.* **91**, 157201 (2003).
- [31] H. Jang, B. Y. Kang, B. K. Cho, M. Hashimoto, D. Lu, C. A. Burns, C.-C. Kao, and J.-S. Lee, *Phys. Rev. Lett.* **117**, 216404 (2016).
- [32] F. Reinert, G. Nicolay, S. Schmidt, D. Ehm, and S. Hüfner, *Phys. Rev. B* **63**, 115415 (2001).
- [33] G. Nicolay, F. Reinert, S. Hüfner, and P. Blaha, *Phys. Rev. B* **65**, 033407 (2001).
- [34] F. Gerken, J. Barth, and C. Kunz, *Phys. Rev. Lett.* **47**, 993 (1981).
- [35] O.-P. Sairanen and S. Aksela, *Journal of Physics: Condensed Matter* **4**, 3337 (1992).
- [36] W.-D. Schneider, C. Laubschat, and B. Reihl, *Phys. Rev. B* **27**, 6538 (1983).
- [37] G. Kaindl, A. Höhr, E. Weschke, S. Vandré, C. Schüßler-Langeheine, and C. Laubschat, *Phys. Rev. B* **51**, 7920 (1995).
- [38] H. Krakauer, M. Posternak, and A. J. Freeman, *Phys. Rev. B* **19**, 1706 (1979).
- [39] E. Wimmer, H. Krakauer, M. Weinert, and A. J. Freeman, *Phys. Rev. B* **24**, 864 (1981).
- [40] FLEUR site: <http://www.flapw.de>.
- [41] V. I. Anisimov, F. Aryasetiawan, and A. I. Lichtenstein, *Journal of Physics: Condensed Matter* **9**, 767 (1997).
- [42] A. B. Shick, A. I. Lichtenstein, and W. E. Pickett, *Phys. Rev. B* **60**, 10763 (1999).
- [43] V. I. Anisimov, I. V. Solovyev, M. A. Korotin, M. T. Czyżyk, and G. A. Sawatzky, *Phys. Rev. B* **48**, 16929 (1993).

- [44] J. P. Perdew, K. Burke, and M. Ernzerhof, *Phys. Rev. Lett.* **77**, 3865 (1996).
- [45] M. Weinert, R. E. Watson, and J. W. Davenport, *Phys. Rev. B* **32**, 2115 (1985).
- [46] C. Li, A. J. Freeman, H. J. F. Jansen, and C. L. Fu, *Phys. Rev. B* **42**, 5433 (1990).
- [47] G. H. O. Daalderop, P. J. Kelly, and M. F. H. Schuurmans, *Phys. Rev. B* **41**, 11919 (1990).
- [48] D.-s. Wang, R. Wu, and A. J. Freeman, *Phys. Rev. B* **47**, 14932 (1993).
- [49] M. Methfessel and A. T. Paxton, *Phys. Rev. B* **40**, 3616 (1989).
- [50] F. Gerken, *Journal of Physics F: Metal Physics* **13**, 703 (1983).
- [51] W. D. Schneider, C. Laubschat, G. Kalkowski, J. Haase, and A. Puschmann, *Phys. Rev. B* **28**, 2017 (1983).
- [52] Y. Que, Y. Zhuang, Z. Liu, C. Xu, B. Liu, K. Wang, S. Du, and X. Xiao, *The Journal of Physical Chemistry Letters* **11**, 4107 (2020).
- [53] See Supplemental Material at ([URL to be provided](#)), which includes additional Refs. [70–72], for further details.
- [54] A. Arrott, *Phys. Rev.* **108**, 1394 (1957).
- [55] S. Danzenbächer, D. V. Vyalikh, Y. Kucherenko, A. Kade, C. Laubschat, N. Caroca-Canales, C. Krellner, C. Geibel, A. V. Fedorov, D. S. Dessau, R. Follath, W. Eberhardt, and S. L. Molodtsov, *Phys. Rev. Lett.* **102**, 026403 (2009).
- [56] E. Abate and M. Asdente, *Phys. Rev.* **140**, A1303 (1965).
- [57] C. Elsasser, M. Fahnle, E. H. Brandt, and M. C. Bohm, *Journal of Physics F: Metal Physics* **18**, 2463 (1988).
- [58] H. Takayama, K.-P. Bohnen, and P. Fulde, *Phys. Rev. B* **14**, 2287 (1976).
- [59] P. Bruno, *Phys. Rev. B* **39**, 865 (1989).
- [60] M. Cinal, D. M. Edwards, and J. Mathon, *Phys. Rev. B* **50**, 3754 (1994).
- [61] G. van der Laan, *Journal of Physics: Condensed Matter* **10**, 3239 (1998).
- [62] L. Ke and M. van Schilfhaarde, *Phys. Rev. B* **92**, 014423 (2015).
- [63] O. Šipr, S. Mankovsky, S. Polesya, S. Bornemann, J. Minár, and H. Ebert, *Phys. Rev. B* **93**, 174409 (2016).
- [64] M. Blanco-Rey, J. I. Cerdá, and A. Arnau, *New Journal of Physics* **21**, 073054 (2019).
- [65] G. H. O. Daalderop, P. J. Kelly, and M. F. H. Schuurmans, *Phys. Rev. B* **50**, 9989 (1994).
- [66] T. Moos, W. Hübner, and K. Bennemann, *Solid State Communications* **98**, 639 (1996).
- [67] A. Lessard, T. H. Moos, and W. Hübner, *Phys. Rev. B* **56**, 2594 (1997).
- [68] P. Ravindran, A. Kjekshus, H. Fjellvåg, P. James, L. Nordström, B. Johansson, and O. Eriksson, *Phys. Rev. B* **63**, 144409 (2001).
- [69] B. Feng, R.-W. Zhang, Y. Feng, B. Fu, S. Wu, K. Miyamoto, S. He, L. Chen, K. Wu, K. Shimada, T. Okuda, and Y. Yao, *Phys. Rev. Lett.* **123**, 116401 (2019).
- [70] B. T. Thole, G. van der Laan, J. C. Fuggle, G. A. Sawatzky, R. C. Karnatak, and J.-M. Esteve, *Phys. Rev. B* **32**, 5107 (1985).
- [71] T. Kinoshita, H. Gunasekara, Y. Takata, S.-i. Kimura, M. Okuno, Y. Haruyama, N. Kotsugi, K. Nath, H. Wada, A. Mitsuda, M. Shiga, T. Okuda, A. Harasawa, H. Ogasawara, and A. Kotani, *Journal of the Physical Society of Japan* **71**, 148 (2002).
- [72] A. Tcakaev, V. B. Zabolotnyy, C. I. Fornari, P. Rüßmann, T. R. F. Peixoto, F. Stier, M. Dettbarn, P. Kagerer, E. Weschke, E. Schierle, P. Bencok, P. H. O. Rappl, E. Abramof, H. Bentmann, E. Goering, F. Reinert, and V. Hinkov, *Phys. Rev. B* **102**, 184401 (2020).

Supplemental Material for: “Valence state determines the band magnetocrystalline anisotropy in 2D rare-earth/noble-metal compounds”

M. Blanco-Rey,^{1,2} R. Castrillo-Bodero,³ K. Ali,^{2,3} P. Gargiani,⁴ F. Bertran,⁵
 P. M. Sheverdyaeva,⁶ J.E. Ortega,^{2,3,7} L. Fernandez,^{3,7} and F. Schiller^{2,3}

¹ Departamento de Polímeros y Materiales Avanzados: Física, Química y Tecnología, Universidad del País Vasco UPV-EHU, 20018 San Sebastián, Spain

² Donostia International Physics Center, E-20018 Donostia-San Sebastián, Spain

³ Centro de Física de Materiales CSIC/UPV-EHU-Materials Physics Center, E-20018 San Sebastián, Spain

⁴ ALBA Synchrotron Light Source, Carretera BP 1413 km 3.3, 08290 Cerdanyola del Vallès, Spain

⁵ Synchrotron SOLEIL, CNRS-CEA, L’Orme des Merisiers, Saint-Aubin-BP48, 91192 Gif-sur-Yvette, France

⁶ Istituto di Struttura della Materia, Consiglio Nazionale delle Ricerche, 34149 Trieste, Italy

⁷ Departamento de Física Aplicada I, Universidad del País Vasco UPV/EHU, E-20018 San Sebastián, Spain

(Dated: January 26, 2022)

S1. ADDITIONAL PHOTOEMISSION RESULTS

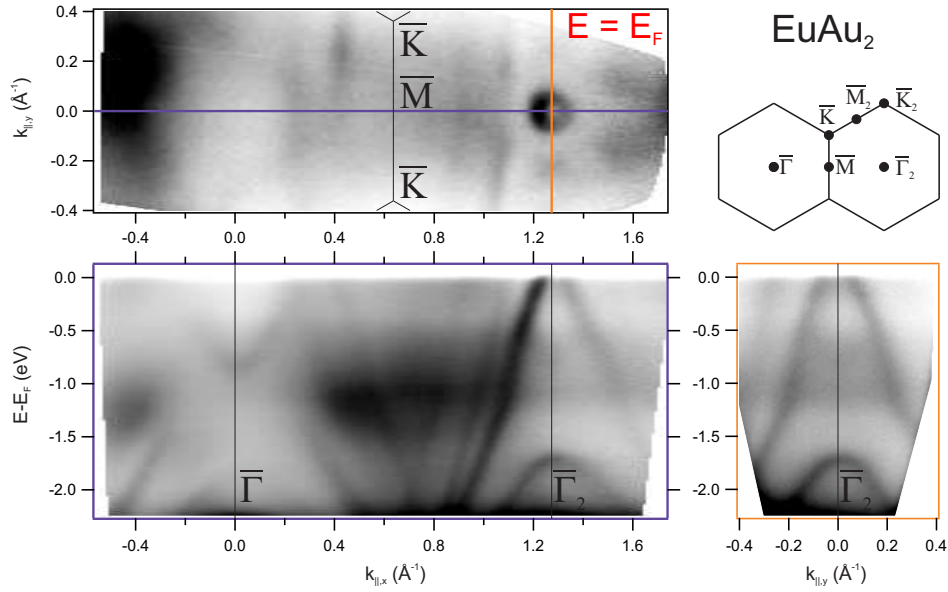


FIG. S1. ARPES intensity mappings of EuAu_2 at $h\nu = 21.2$ eV. Fermi energy intensity plot (Fermi surface mapping) of the EuAu_2 surface and band structure cuts along the $\bar{\Gamma}\bar{M}\bar{\Gamma}_2$ and $\bar{K}_2\bar{\Gamma}_2\bar{K}_2$ surface Brillouin zone directions.

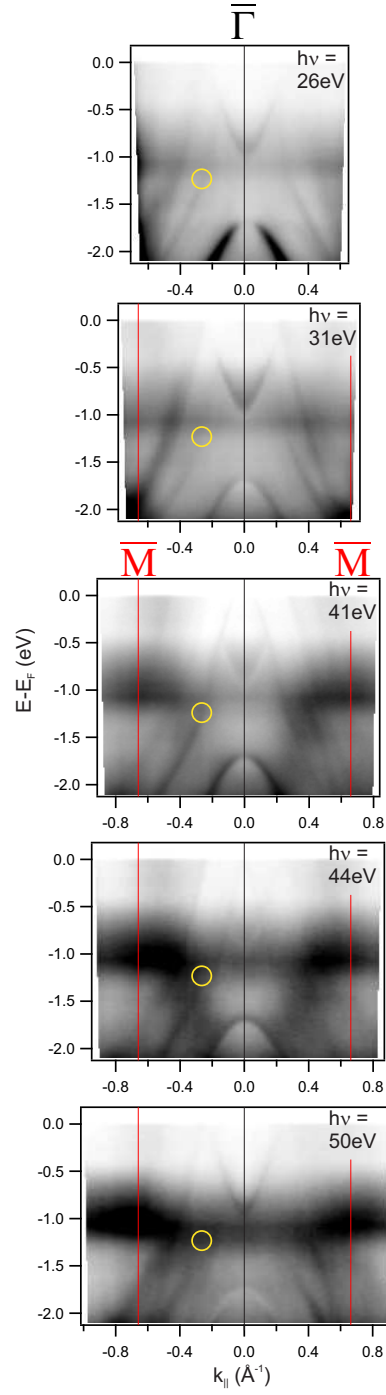


FIG. S2. **ARPES intensity plots along the $\bar{M}\bar{\Gamma}\bar{M}$ high symmetry direction in EuAu_2 .** Photoemission intensity mappings along the $\bar{\Gamma}_2\bar{M}\bar{\Gamma}\bar{M}\bar{\Gamma}_2$ high symmetry line. The yellow circle at -0.27 \AA^{-1} and -1.2 eV reveal that the observed kink in the C band does not disperse for different photon energies.

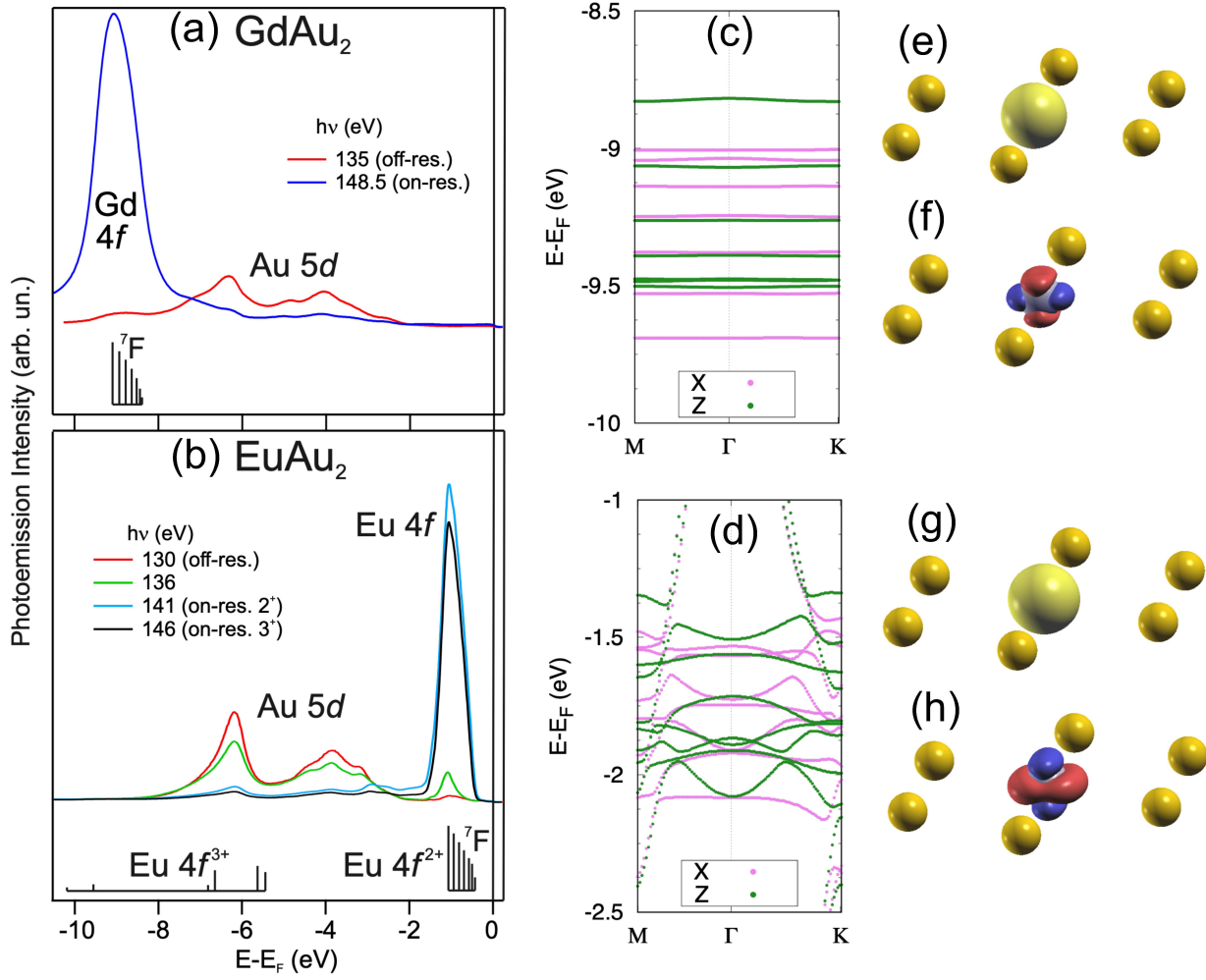


FIG. S3. **Electronic structure of the 4f states in free-standing GdAu₂ and EuAu₂.** (a,b) Off- and on-resonant photoemission of GdAu₂ and EuAu₂, respectively, obtained at the indicated photon energies. The indicated multiplets are taken from Refs. [1, 2]. (c,d) Detail of the self-consistently calculated spin-orbit-split 4f bands of free-standing GdAu₂ (c) and EuAu₂ (d) for spins oriented along the X (purple) or Z (green) directions. Note the contrast between the weak dispersion and strong hybridization of the GdAu₂ and EuAu₂ cases, respectively. (e,g) Real-space representations of the RE(4f) charge density $\rho(\mathbf{r})$, obtained from the integration of the Kohn-Sham states with spins along the Z direction shown in panels (c) and (d), respectively. The depicted isoelectronic surface is $0.1 ea_0^{-3}$. In both atoms, the deviation from sphericity are negligible by bare eye. The next quantity can, in contrast, probe the asphericity of the orbital with more precision. (f,h) Real-space representations of the anisotropy of the 4f magnetization density, calculated as $\Delta m(\mathbf{r}) = m_X(\mathbf{r}) - m_Z(\mathbf{r})$, with red (blue) indicating $\Delta m(\mathbf{r}) > 0$ (< 0). The depicted isosurfaces in this case are $0.0001 ea_0^{-3}$ for Gd(4f) (g) and $0.001 ea_0^{-3}$ for Eu(4f) (h). The $m^{\text{Gd}}(\mathbf{r})$ sensitivity to the magnetization axis is smaller than that of $m^{\text{Eu}}(\mathbf{r})$ by an order of magnitude, which means that Eu(4f) is more prone to be deformed by a magnetic field, i.e. it can provide non-negligible contributions to the MAE by departure of its spherical shape, as shown in the main paper Fig. 4.

S2. ADDITIONAL XAS RESULTS

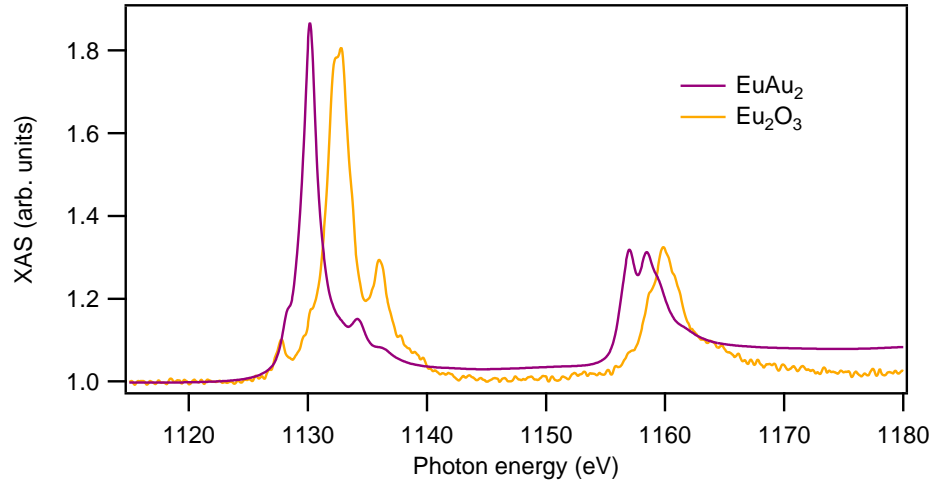


FIG. S4. X-ray absorption spectra taken with linear horizontal polarized light at normal incidence geometry for divalent EuAu_2 and trivalent Eu_2O_3 . X-ray absorption spectroscopy results can be used to easily distinguish di- and tri-valent Eu atoms in compounds. Here we show the spectra of completely divalent Eu in EuAu_2 and trivalent Eu in Eu_2O_3 . For comparison, theoretical and experimental spectra of divalent Eu atoms in different compounds can be found in Refs. [3–5].

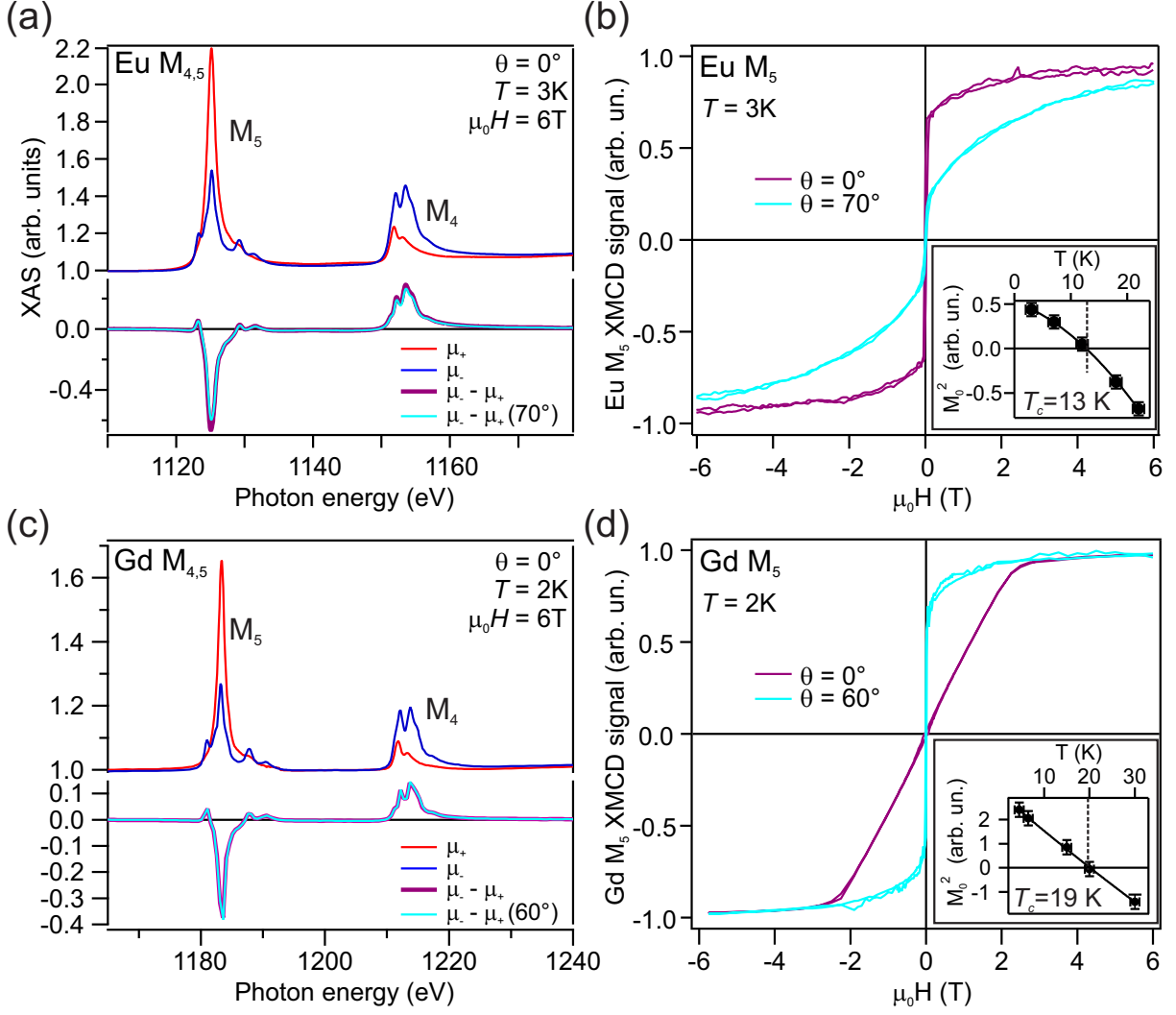


FIG. S5. **Comparison of the magnetic properties of EuAu₂ and GdAu₂.** (a),(c) X-ray absorption spectra taken with left and right polarized light at $T = 3\text{K}$ and $T = 2\text{K}$ and with an applied field of $\mu_0 H = 6\text{T}$ with the field applied normal to the surface for EuAu₂ and GdAu₂, respectively. The resulting difference, the XMCD signals, are shown in the bottom part for fields normal to the surface $\theta = 0^\circ$, at $\theta = 70^\circ$ and 60° , respectively. (b),(d) The magnetization curves are obtained by acquisition of the XAS signal at the maximum of the XMCD signal (and a pre-edge value for normalization) varying continually the applied field from $+6\text{T}$ to -6T and then from -6T to $+6\text{T}$ for both circular light polarizations. The Curie temperature T_C can be extracted by the Arrott plot analysis [6, 7] of magnetization curves taken at several temperatures around T_C . As a result we obtain $T_C = 13\text{K}$ and 19K for the EuAu₂ and GdAu₂ surface compounds, respectively. Most important here is the change in the anisotropy, resulting in an out-of-plane easy axis of magnetization for Eu atoms in EuAu₂ and an in-plane easy axis for Gd in GdAu₂.

S3. TESTS ON THE VALIDITY OF THE FORCE THEOREM APPROACH

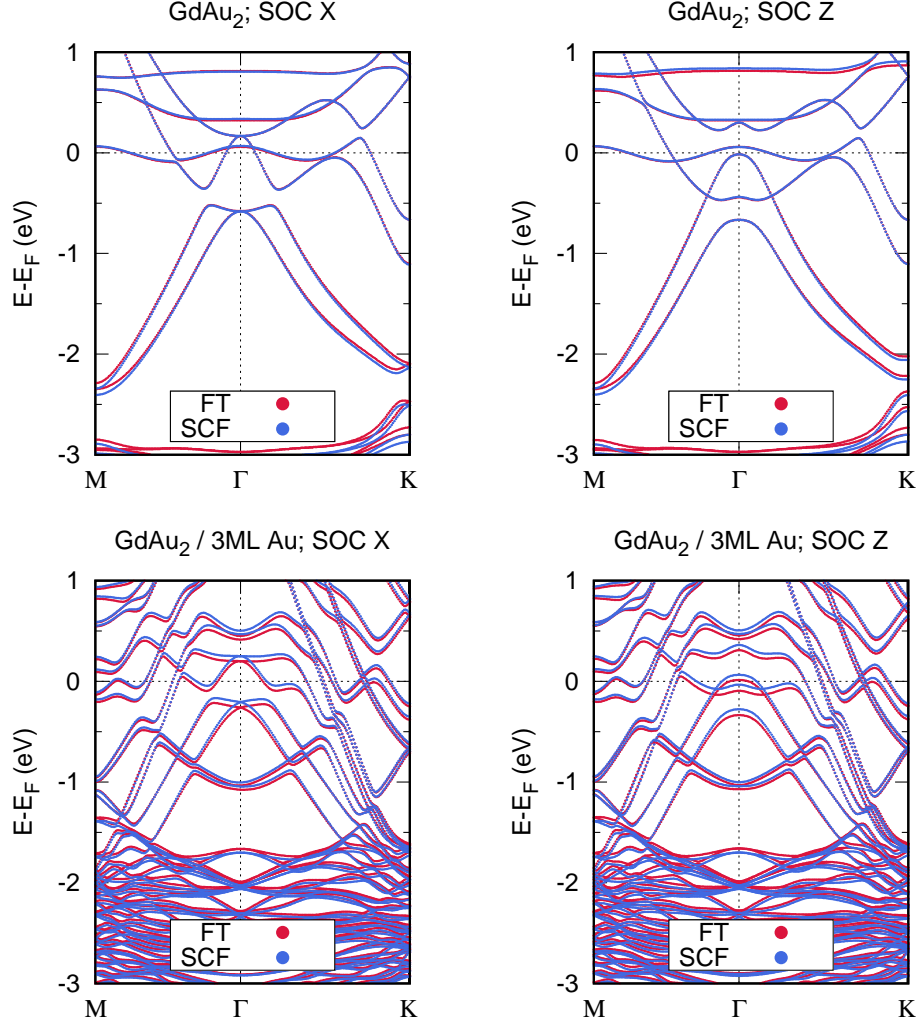


FIG. S6. **Self-consistent and force-theorem bands for free-standing and supported GdAu₂ structures.** Band structures of free-standing and supported GdAu₂ are shown for spins aligned to in-plane (panels labelled as SOC X) and out-of-plane (SOC Z) directions. The eigenenergies obtained for SOC included in the force theorem approximation (labelled FT, red) are compared with the self-consistent ones (SCF, blue). Each individual calculation is referred to its own Fermi level (note that the Fermi energy changes if the spin orientation changes). Agreement between FT and SCF calculations in the case of a 3ML Au substrate is reduced with respect to that of free-standing GdAu₂ due to the intense SOC at the substrate bands, which introduces small overall shifts in the band structure. Despite this, the overall band structure, and in particular the gap openings, for the two spin directions are satisfactorily reproduced by the force theorem method.

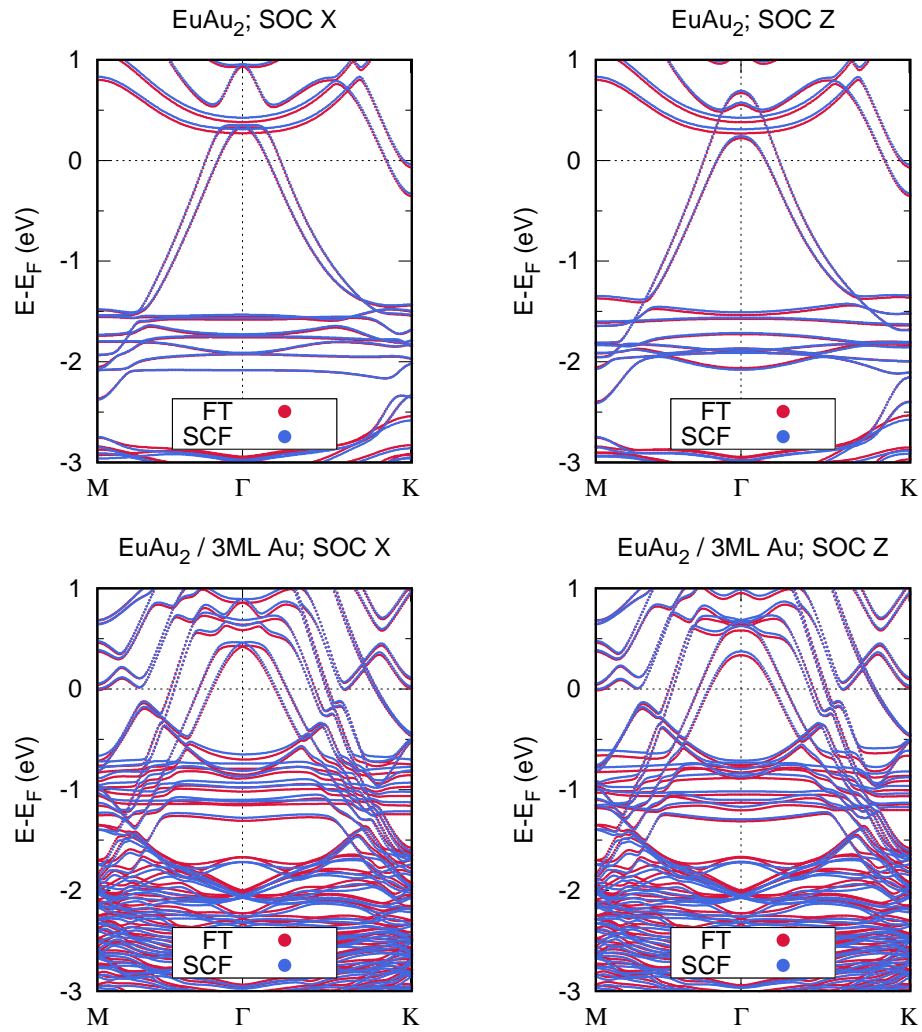


FIG. S7. Self-consistent and force-theorem bands for free-standing and supported EuAu₂ structures. Same information as in Fig. S6 for the EuAu₂ case.

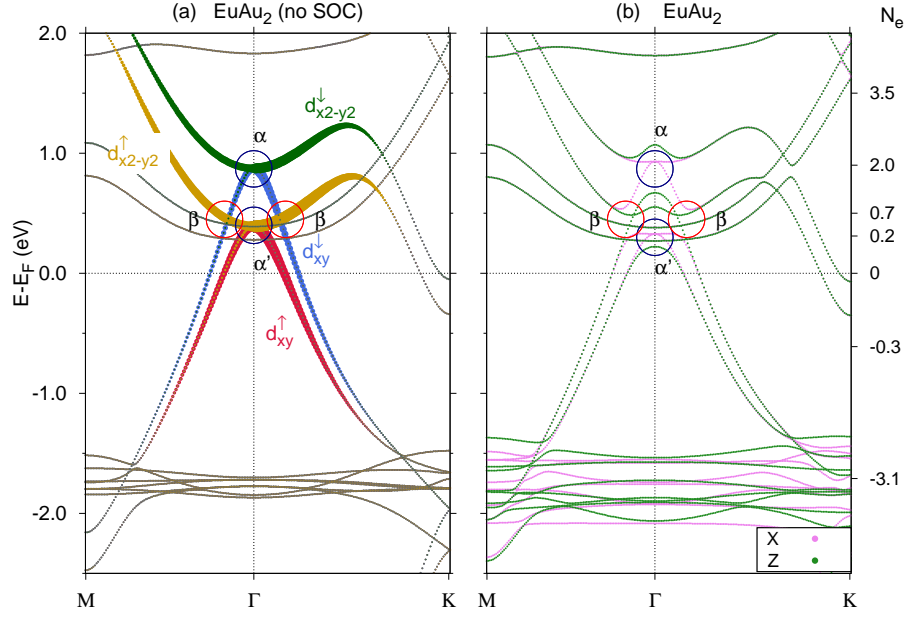


FIG. S8. **Band structure for free-standing EuAu₂.** (a) To guide the eye, orbital and spin characters of free-standing EuAu₂ bands in the absence of SOC. (b) Band structure of free-standing EuAu₂ with SOC (force theorem) for spins aligned to the X (violet) and Z (green) directions. The right-hand side axis shows the corresponding band filling N_e (see also Fig. S9). Note that the gap openings that were relevant in the anisotropy of trivalent GdAu₂ (labelled α , α' and β) lie above the Fermi level in the EuAu₂ case and therefore do not contribute to the observed MAE.

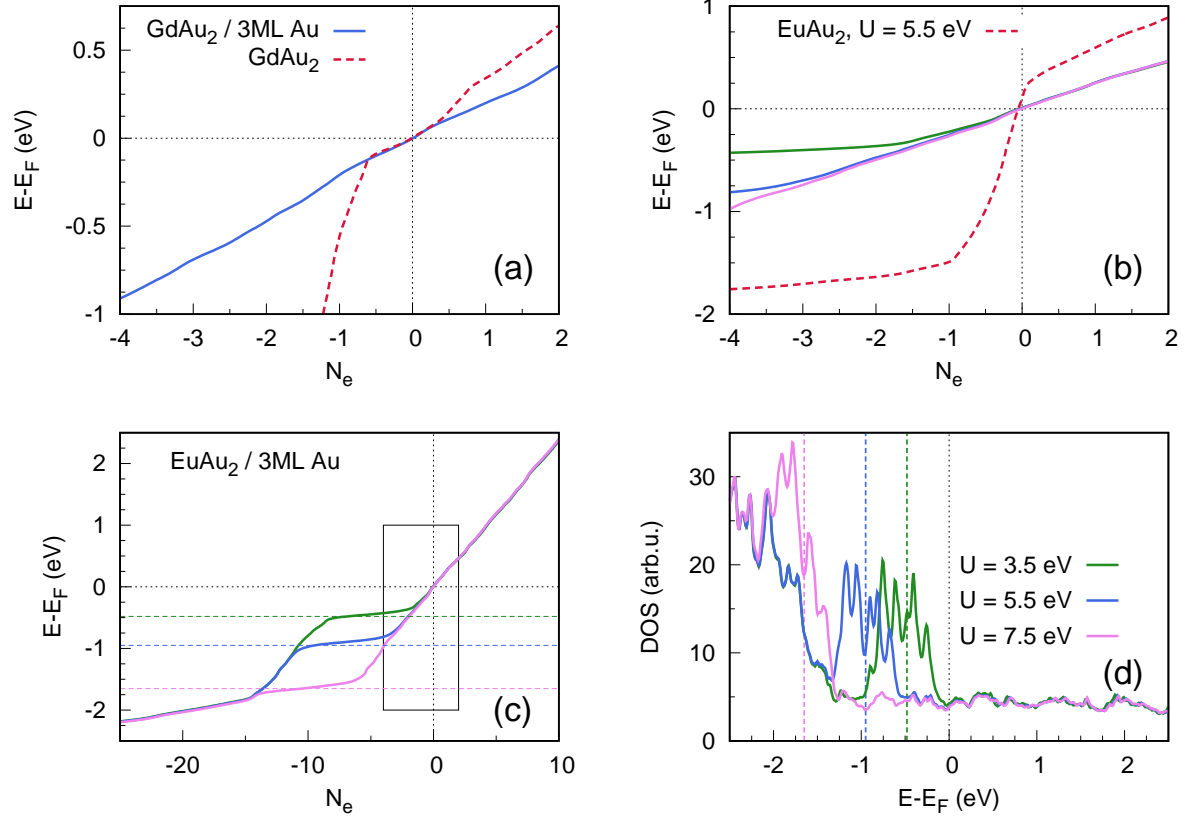
S4. VISUAL GUIDE TO INTERPRET THE MAE(N_e) CURVES

FIG. S9. **Correspondence between N_e and Fermi energies. Dependence of $\text{EuAu}_2 / 3\text{ML Au}$ electronic structure and MAE with the correlation parameter.** (a-c) Guides to the eye to interpret the MAE(N_e) curves in the main paper. The curves represent the Fermi energy that corresponds to a given filling with respect to neutrality ($N_e = 0$), as in the right-hand axis ticks of main paper Figs. 3(b,c). These fillings are calculated as an integral of the density of states for each one of the four considered systems without including SOC. (a) free-standing and supported GdAu_2 to interpret the MAE(N_e) curves of Fig. 3(d). (b) Same for EuAu_2 [Fig. 4(a)]. (c) A wider range of fillings allows to identify the $\text{Eu}(4f)$ contributions in Fig. 4(b), located at different binding energies (indicated by horizontal dashed lines) or N_e interval (plateaus) depending on the U values. The $4f$ broadened band is displaced toward the Fermi level for lower U values. (d) Total density of states calculated for $\text{EuAu}_2 / 3\text{ML Au}$ with spins perpendicular to the surface in the force theorem approximation for three values of the correlation parameter U . For $U = 5.5$ eV (blue), the broad peak centered at energies $E - E_F \approx -1$ eV corresponds to the hybridized $4f$ bands, in agreement with the experimental binding energies. For $U = 7.5$ eV (purple) the $4f$ band lies at the top of Au substrate d band.

-
- [1] F. Gerken, *Journal of Physics F: Metal Physics* **13**, 703 (1983).
 - [2] W.-D. Schneider, C. Laubschat, and B. Reihl, *Phys. Rev. B* **27**, 6538 (1983).
 - [3] B. T. Thole, G. van der Laan, J. C. Fuggle, G. A. Sawatzky, R. C. Karnatak, and J.-M. Esteve, *Phys. Rev. B* **32**, 5107 (1985).
 - [4] T. Kinoshita, H. Gunasekara, Y. Takata, S.-i. Kimura, M. Okuno, Y. Haruyama, N. Kosugi, K. Nath, H. Wada, A. Mitsuda, M. Shiga, T. Okuda, A. Harasawa, H. Ogasawara, and A. Kotani, *Journal of the Physical Society of Japan* **71**, 148 (2002).
 - [5] A. Tcakaev, V. B. Zabolotnyy, C. I. Fornari, P. Rüßmann, T. R. F. Peixoto, F. Stier, M. Dettbarn, P. Kagerer, E. Weschke, E. Schierle, P. Bencok, P. H. O. Rappl, E. Abramof, H. Bentmann, E. Goering, F. Reinert, and V. Hinkov, *Phys. Rev. B* **102**, 184401 (2020).
 - [6] A. Arrott, *Phys. Rev.* **108**, 1394 (1957).
 - [7] M. Ormaza, L. Fernández, M. Ilyn, A. Magaña, B. Xu, M. J. Verstraete, M. Gastaldo, M. A. Valbuena, P. Gargiani, A. Mugarza, A. Ayuela, L. Vitali, M. Blanco-Rey, F. Schiller, and J. E. Ortega, *Nano Letters* **16**, 4230 (2016).